

TYPE IA SUPERNOVAE FROM MERGING WHITE DWARFS I) PROMPT DETONATIONS

R. MOLL^{1,4}, C. RASKIN², D. KASEN^{2,3} AND S. E. WOOSLEY¹

(Dated: September 3, 2021)
Draft version September 3, 2021

ABSTRACT

Merging white dwarfs are a possible progenitor of Type Ia supernovae (SNe Ia). While it is not entirely clear if and when an explosion is triggered in such systems, numerical models suggest that a detonation might be initiated before the stars have coalesced to form a single compact object. Here we study such “peri-merger” detonations by means of numerical simulations, modeling the disruption and nucleosynthesis of the stars until the ejecta reach the coasting phase. Synthetic light curves and spectra are generated for comparison with observations. Three models are considered with primary masses $0.96 M_{\odot}$, $1.06 M_{\odot}$, and $1.20 M_{\odot}$. Of these, the $0.96 M_{\odot}$ dwarf merging with an $0.81 M_{\odot}$ companion, with a ^{56}Ni yield of $0.58 M_{\odot}$, is the most promising candidate for reproducing common SNe Ia. The more massive mergers produce unusually luminous SNe Ia with peak luminosities approaching those attributed to “super-Chandrasekhar” mass SNe Ia. While the synthetic light curves and spectra of some of the models resemble observed SNe Ia, the significant asymmetry of the ejecta leads to large orientation effects. The peak bolometric luminosity varies by more than a factor of 2 with the viewing angle, and the velocities of the spectral absorption features are lower when observed from angles where the light curve is brightest. The largest orientation effects are seen in the ultraviolet, where the flux varies by more than an order of magnitude. Despite the large variation with viewing angle, the set of three models roughly obeys a width-luminosity relation, with the brighter light curves declining more slowly in the B-band. Spectral features due to unburned carbon from the secondary star are also seen in some cases.

Subject headings: hydrodynamics – nuclear reactions, nucleosynthesis, abundances – shock waves – supernovae: general – white dwarfs

1. INTRODUCTION

It is generally believed that the progenitors of type Ia supernovae (SNe Ia) are the explosion of carbon-oxygen white dwarfs (WDs) powered by thermonuclear fusion. There is currently no consensus, however, regarding the events leading to the explosion. Models of SNe Ia progenitor systems are generally classified as either “single-degenerate” or “double-degenerate”, depending on whether the progenitor system consists of one WD and a non-degenerate companion, or two WDs. Single-degenerate scenarios are further divided into Chandrasekhar mass models (for a review, see Hillebrandt & Niemeyer 2000) and sub-Chandrasekhar mass models (e.g. Woosley & Kasen 2011), depending on the mass of the exploding star. Detonations of sub-Chandrasekhar mass WDs may be triggered by the explosion of a helium shell, which ignites more readily than the carbon-oxygen mixture out of which the core WD is assumed to be composed (Fink et al. 2007, 2010; Sim et al. 2012; Shen & Bildsten 2013; Moll & Woosley 2013).

In the double-degenerate scenario, two WDs merge and explode, an idea suggested 30 years ago as a possible progenitor for SNe Ia (Iben & Tutukov 1984; Webbink 1984). This scenario can naturally explain the lack of

hydrogen spectral lines in SNe Ia, and is supported by studies of stellar population synthesis (Ruiter et al. 2011, 2013). The merger starts when the lighter of the two stars overflows its Roche lobe. The ensuing mass transfer is often unstable (Marsh et al. 2004), leading to the rapid disruption of the less massive star (e.g., Benz et al. 1990; Yoon et al. 2007).

Recent simulations have shown that detonations leading to SNe Ia could be triggered relatively early in the merging process. Pakmor et al. (2011) explored the coalescence of $\approx 0.90 M_{\odot}$ WDs with secondaries between $0.70 M_{\odot}$ and $0.89 M_{\odot}$. For secondary masses down to $0.76 M_{\odot}$, they found conditions favorable for a detonation during the early phases of the merger. In the case of two $0.89 M_{\odot}$ WDs, they followed the merger, detonation and the subsequent explosion, finding that the model synthesized a relatively small amount of ^{56}Ni and resembled the class of sub-luminous, 1991bg-like SNe Ia (Pakmor et al. 2010). Mergers that included a higher mass WD, $M \simeq 1.1 M_{\odot}$, produced more ^{56}Ni and might yield a more normal SN Ia (Pakmor et al. 2012b,a). Models of a $(1.1 + 0.9)M_{\odot}$ merger provided a reasonable match to the light curves and spectra of SN 2011fe (Röpke et al. 2012).

The possibility of such “peri-merger detonations” (i.e., detonations set off during the merging process) is disputed in the literature. Guerrero et al. (2004) conclude that the formation of an SN Ia during the merger is unlikely. The parameter study of Dan et al. (2012) also argues against such an outcome in the case of pure carbon-oxygen WDs. However, the resolution in these studies was low compared to other recent merger calculations

¹ Department of Astronomy and Astrophysics, University of California, Santa Cruz, CA 95064, USA

² Nuclear Science Division, Lawrence Berkeley National Laboratory, Berkeley, CA 94720, USA

³ Department of Physics and Astronomy, University of California, Berkeley, CA 94720, USA

⁴ Max-Planck-Institut für Astrophysik, Karl-Schwarzschild-Str. 1, 85748 Garching, Germany

TABLE 1
MASSES [M_{\odot}] AT DIFFERENT DENSITIES AT THE
BEGINNING OF THE DETONATION SIMULATIONS

	ρ [g cm^{-3}] ↓	1.20 + 1.06	1.06 + 1.06	0.96 + 0.81
primary	$> 10^5$	~ 1.406	~ 1.222	~ 0.993
	$> 2 \times 10^6$	~ 1.280	~ 1.101	0.853
	$> 5 \times 10^6$	1.177	0.922	0.666
	$> 10^7$	1.069	0.738	0.430
	$> 2 \times 10^7$	0.935	0.475	0.133
secondary	$> 10^5$	~ 0.638	~ 0.792	~ 0.521
	$> 2 \times 10^6$	~ 0.339	~ 0.579	0.160
	$> 5 \times 10^6$	0.002	0.257	0.000
	$> 10^7$	0.000	0.006	0.000

(Raskin et al. 2012; Zhu et al. 2013), and this has likely played a role in the disparate conclusions. If the merger does not lead to an early thermonuclear runaway, it will ultimately make a single compact object surrounded by a disk (e.g., Lorén-Aguilar et al. 2009). We shall consider the possibility of explosions in this post-merger state in a separate paper (Raskin et al. 2013).

In this work, we study the possibility and consequences of peri-merger detonations. §2 describes the merger setups and our detonation conditions. §3 presents the resulting yields and ejecta morphology. §4 discusses radiative transport calculations of the synthetic light curves and spectra carried out for azimuthally averaged models. §4 summarizes our findings and discusses avenues for further study.

2. METHODS

2.1. Merging and Initial Models

To simulate the merger phase of the calculation, we use the smoothed particle hydrodynamics code SNSPH (Fryer et al. 2006). Following procedures laid out in Raskin et al. (2012) for generating initial conditions, we ensure accurate mass transfer rates consistent with the results of Dan et al. (2012). When our merger simulations approach the detonation conditions of Seitenzahl et al. (2009), we interpolate an earlier SNSPH snapshot onto a uniform Cartesian grid at three different resolutions, corresponding to different levels of refinement. We then evolve the system with the Eulerian grid code CASTRO (see the next section). Figure 1 presents an overview of the snapshots that were followed up with CASTRO. The hottest regions are located near the orbital plane ($|z| \lesssim \pm 1$ Mm) where the accretion stream from the secondary star impacts the surface of the primary, see the red contours in the plots. Shortly after the simulations are restarted in CASTRO, detonations spontaneously commence at one or several points in these regions. Looking down the z -axis as in Figure 1, the stars are rotating around a common center (close to the primary) in counter-clockwise direction. We refer to this general direction of rotation in the description of the results when stating that something is “ahead” or “behind” one of the stars.

Due to inconsistencies in the way SNSPH and CASTRO handle shock physics, the precise times and locations where detonation conditions are reached are not identical after the code-swap. However, since an appreciable amount of material is reaching detonation conditions at roughly the same time in the SNSPH

simulation—as is demonstrated by the red contours in the mapped CASTRO snapshots in Figure 1—this slight variation should not affect the outcome. With the exception of model 0.96 + 0.81, the largest disparity in times between detonation conditions being reached in the two codes is ~ 5 s.

One of the models, 0.96 + 0.81, does not ignite in CASTRO. After mapping the SPH data onto the Cartesian grid, the hottest spot in the orbital plane has a temperature of 1.26×10^9 K, and a density of 1.32×10^6 g cm $^{-3}$ at the highest level of refinement, corresponding to $3.5 \times 10^{-8} M_{\odot}$ in that zone. The hottest point overall is 1069 km away from the orbital plane, and has a temperature of 1.51×10^9 K, but the density there is only 0.88×10^6 g cm $^{-3}$. These spots do not induce a detonation in CASTRO, even with a full 19-isotope network (running with a full network avoids the lower temperature limit of our tables), and no higher temperatures develop in the course of the following 10 seconds in the orbital plane. As argued above, we expect the switch from SNSPH to CASTRO, and the interpolation of the data onto a grid, to have an unavoidable impact on the thermal evolution. In light of this, we rate the possibility for ignition of this model as uncertain. To force a detonation, we manually put a hot spot with a central temperature of 3×10^9 K and a radius of 300 km at the location of the hottest point in the orbital plane, see the small yellow circle in Figure 1c.

The central densities indicate varying evolutionary states (degree of deformation and mass loss) of the secondary stars at the time of the detonation. For example, the maximum density of the secondary in model 1.20 + 1.06 is only about half as high as in the model 1.06 + 1.06, even though they start out with the same masses. Table 1 lists the masses of gas above a given density cutoff at the beginning of the detonation simulations. The values represent the masses of contiguous regions about the centers of the primary and secondary stars. For low densities, the contiguous regions are identical, and we split the total mass into parts associated with the primary and the secondary by means of a cutting plane, the location of which is determined by eye from the density in the orbital plane. These split values are preceded by a “ \sim ” in the tables. The numbers show that the density of the material in the secondary is relatively low, and that a significant mass transfer has taken place before the detonation.

Even though model 1.06 + 1.06 starts with two WDs of identical mass, a slight geometric asymmetry is sufficient to unbind one of the stars, as was described in Raskin et al. (2012). Since perfectly identical stars in binaries are probably exceedingly rare, we expect this outcome to be more likely in nature.

2.2. Detonation and Explosion

For our 3D detonation study, we use the Eulerian hydrodynamics code CASTRO (Almgren et al. 2010; Zhang et al. 2011) to solve the equations for compressible fluid dynamics in combination with a nuclear reaction network. The equation of state is based on the Helmholtz free energy (Timmes & Arnett 1999; Timmes & Swesty 2000), and the gravitational potential is calculated with a Poisson solver. We use lookup tables based on a 199-isotope network to compute the nuclear energy gen-

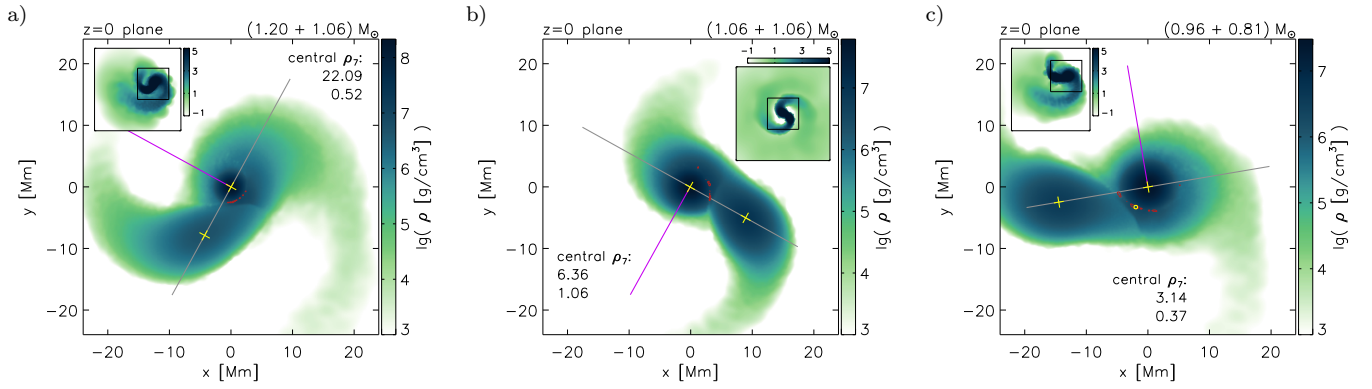


FIG. 1.— Density in the orbital plane at the beginning of the detonation simulations. Yellow crosses mark the density maxima of the two stars, which for clarity are also written inside each plot (in units of 10^7 g cm^{-3}). The denser primary is centered at the coordinate origin. Red contours indicate the hottest regions in the plane (the respective levels are $T_9 = 2.0, 1.2, 0.8$ for panels a, b, and c). The small yellow circle in panel (c) represents the perimeter of the detonator (contours at $T_9 = 2.0$) which is needed to get a detonation going in this model. The insets in each panel show a larger region, with the small black squares indicating the boundaries of the respective main plot. The gray and magenta lines indicate axes in the orbital plane that are used in the description of the results.

TABLE 2
 ^{56}Ni YIELDS [M_\odot] FOR BARE CARBON-OXYGEN WDs WITH
DIFFERENT CODES AND NETWORKS

	$1.1 M_\odot$	$1.0 M_\odot$	$0.9 M_\odot$	$0.8 M_\odot$
KEPLER 19-iso ^a	0.791	0.488	0.166	0.0167
CASTRO 19-iso	0.769	0.473	0.160	0.0118
KEPLER 199-iso ^b	0.825	0.566	0.287	0.0551
CASTRO table ^c	0.748	0.517	0.271	0.0668

^a using a 19-isotope network

^b using a 199-isotope network directly

^c using a table based on the 199-isotope network

eration and element synthesis, with the yields packed into 19 isotopes. In dense ($\rho > 10^6 \text{ g cm}^{-3}$), carbon-rich ($X_C > 0.1$) zones with temperatures greater than $1.5 \times 10^9 \text{ K}$, the composition changes and energy release from carbon burning are determined from the table. Once the temperature has risen above $2.1 \times 10^9 \text{ K}$ in a zone, another table is used to determine the final, freeze-out composition. To prevent a spurious propagation of the detonation through mixing with hot ash, this last step is only allowed if burning conditions in a particular zone are met for at least half a sound crossing time. The accuracy of the tables in CASTRO was confirmed on a set of bare carbon-oxygen WDs by comparison with the KEPLER code (Woosley & Kasen 2011), see Table 2. The stars in these 1D tests were resolved by approximately 160 radial zones in CASTRO, which is roughly similar to the 3D resolution used for the merger detonations. We find reasonable agreement between 199-isotope network simulations in KEPLER and simulations with the tables in CASTRO. The small network is much less efficient in producing ^{56}Ni in low-mass WDs.

The detonation simulations are started with 3 levels of static mesh refinement. Each level consists of a cube centered on the point of highest density. The domain sizes are $(12 \times 10^8 \text{ cm})^3$, $(48 \times 10^8 \text{ cm})^3$ and $(192 \times 10^8 \text{ cm})^3$. The grid is resolved with $320 \times 320 \times 320$ zones at each level. The innermost level is dropped when the detonation reaches the refinement boundary. Once the ejecta gets near outer boundary, we map the data into a new domain twice as large, dropping the innermost level of refinement. This step is repeated until the ejecta gets near the boundary of a domain of $(3.07 \times 10^{11} \text{ cm})^3$, at

which time the expansion is largely homologous in all cases considered, and the internal energy is only a small fraction ($< 0.5\%$) of the kinetic energy.

Unlike the SPH simulations used for calculating the merging process, CASTRO is unable to handle vacua. The density of the ambient medium was set to $10^{-1} \text{ g cm}^{-3}$ at the beginning, and lowered by factors of 10 down to $10^{-4} \text{ g cm}^{-3}$ during remaps into bigger domains (to fill the volume not covered by the old domain). For comparison, the highest densities at the end of the simulations are $> 20 \text{ g cm}^{-3}$ in all cases. Low-density material is being swept up at the explosion front, but appears to have no impact on the much denser bulk of the ejecta inside, which expands homologously. The total mass of the ambient medium filling empty regions is always smaller than $1.9 \times 10^{-3} M_\odot$.

To increase the numerical stability during the shock breakout and to contain detrimental effects on the time step, we employed a velocity cap of $3 \times 10^9 \text{ cm s}^{-1} \approx 0.1c$. We kept track of the kinetic energy thus subtracted from the system. The total subtracted energies are smaller than 1.2% of the total energy at the end of the simulations in all cases.

3. RESULTS

3.1. Detonations

In all of the models, detonation waves emerge shortly ($< 0.1 \text{ s}$) after the simulations are resumed in CASTRO at the state depicted in Figure 1. The primary star is consumed by the detonation on a time scale of half a second, see Figure 2 for an example. The system rotates only a few degrees during that time. While a shock wave moves through the secondary star, it does not produce additional ^{56}Ni . However, some ^{28}Si is produced in association with the secondary and/or the accretion stream it feeds⁵.

The shape of the ejecta is governed by the anisotropic density of the medium surrounding the primary. After the detonation has consumed the primary, the shock in the orbital plane accelerates most efficiently in directions ahead of the primary, and least efficiently along the line

⁵ While it is not possible to unambiguously separate the yields of the two stars without tracers, the formation of a ^{28}Si ‘‘lump’’ in the direction of the secondary is evident.

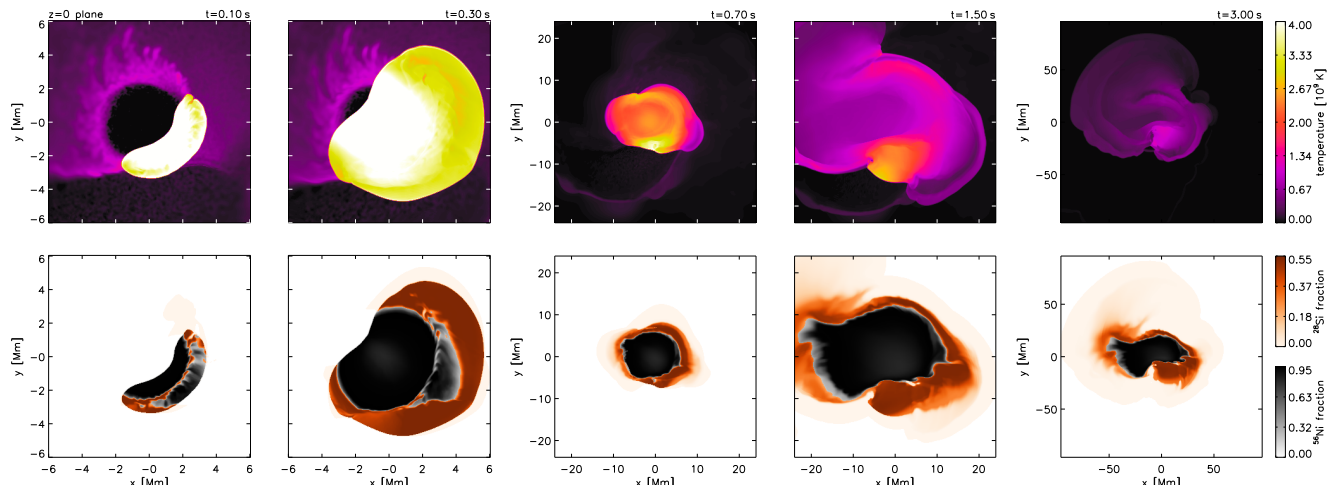


FIG. 2.— Snapshots of the temperature (*top row*) and the mass fractions of ^{56}Ni and ^{28}Si (*bottom row*, ^{56}Ni in black and ^{28}Si in orange colors) in the orbital plane of model 1.20 + 1.06. For the plots in the *bottom row*, only the element with the respective larger mass fraction is plotted at each pixel.

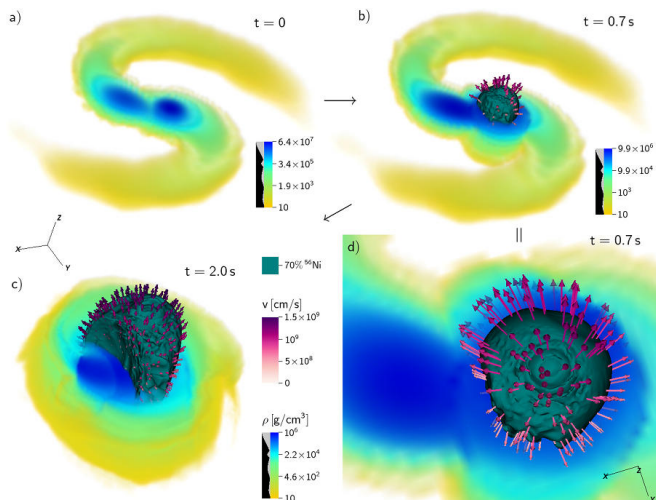


FIG. 3.— Volume renderings of the density in model 1.06 + 1.06 right before the detonation (panel a) and after the consumption of the primary star. The density plot is clipped at the orbital plane, i.e., only half of the volume is shown. The teal isosurface indicates the main pocket of ^{56}Ni . The pink/magenta arrows protruding from this surface represent the fluid velocity on the surface (arrows are scaled by magnitude). Panel (d) shows the same data as panel (b), but at a different perspective and higher zoom level. For a sense of scale: the largest extent of the ^{56}Ni surface is approximately 10^9 cm in panels (b) and (d), and 4.4×10^9 cm in panel (c).

connecting the two stars. As illustrated in Figure 2, this anisotropic acceleration causes the ejecta to become elongated in shape in the orbital plane. The 3D visualization of Figure 3 demonstrates how the acceleration of the ^{56}Ni ejecta is inhibited in some directions, forcing it to become aspherical.

At about three seconds after the start of the detonation, the temperature has become too low for nuclear reactions everywhere. The shapes of the ejecta are still visibly evolving after that, albeit only slightly. We stopped the CASTRO simulations after 48 s, at which time the ejecta are expanding homologously.

3.2. Yields

Table 3 lists the isotope yields of all models. Based on the sum over the masses of all species except for the fuel

TABLE 3
NUCLEOSYNTHESIS YIELDS [M_{\odot}] AND TOTAL ENERGIES [ERG]

model	1.20 + 1.06	1.06 + 1.06	0.96 + 0.81
^4He	3.53×10^{-3}	6.05×10^{-3}	4.46×10^{-3}
^{12}C	0.119	4.42×10^{-2}	0.101
^{14}N	2.29×10^{-13}	3.36×10^{-14}	2.33×10^{-13}
^{16}O	0.448	0.311	0.422
^{20}Ne	2.33×10^{-2}	1.06×10^{-2}	1.06×10^{-2}
^{24}Mg	5.70×10^{-2}	4.32×10^{-2}	4.89×10^{-2}
^{28}Si	0.381	0.485	0.389
^{32}S	0.138	0.269	0.155
^{36}Ar	1.22×10^{-2}	3.20×10^{-2}	1.82×10^{-2}
^{40}Ca	6.78×10^{-3}	2.24×10^{-2}	1.41×10^{-2}
^{44}Ti	6.21×10^{-6}	1.68×10^{-5}	1.32×10^{-5}
^{48}Cr	1.93×10^{-4}	4.10×10^{-4}	3.51×10^{-4}
^{52}Fe	5.22×10^{-3}	8.07×10^{-3}	7.93×10^{-3}
^{54}Fe	7.45×10^{-2}	3.50×10^{-2}	1.78×10^{-2}
^{56}Ni	0.999	0.863	0.580
$28 < A < 40$	0.537	0.808	0.576
$A \geq 44$	1.079	0.906	0.606
E_{begin}	-6.39×10^{50}	-5.17×10^{50}	-3.08×10^{50}
E_{end}	2.24×10^{51}	2.42×10^{51}	1.80×10^{51}
ΔE	2.88×10^{51}	2.94×10^{51}	2.11×10^{51}

elements ^{12}C and ^{16}O , we categorize models 1.20 + 1.06 and 1.06 + 1.06 as super-Chandrasekhar mass detonations, and model 0.96 + 0.81 as sub-Chandrasekhar. The sum of the masses of intermediate-mass elements (IMEs, $28 < A < 40$) and iron-group elements ($A \geq 44$) are listed in a separate row for convenience. The table also lists the total energies (kinetic + internal + gravitational) at the beginning (when the detonation sets off) and end of the simulations, as well as the energy yields.

Figure 4 indicates the location of these yields in the homologously expanding ejecta by plotting the total masses and mass fractions of different elements versus velocity. The mass-weighted mean velocity of the total ejecta is in the range of $(8.8\text{--}9.6) \times 10^8$ cm s $^{-1}$, with the model 1.06 + 1.06 being the fastest, and model 0.96 + 0.81 being the slowest. The mass-weighted mean velocity of the ^{56}Ni ejecta is smaller than that of the IMEs in all cases. Model 0.96 + 0.81 stands out in having a high abundance of IMEs without ^{56}Ni at the center.

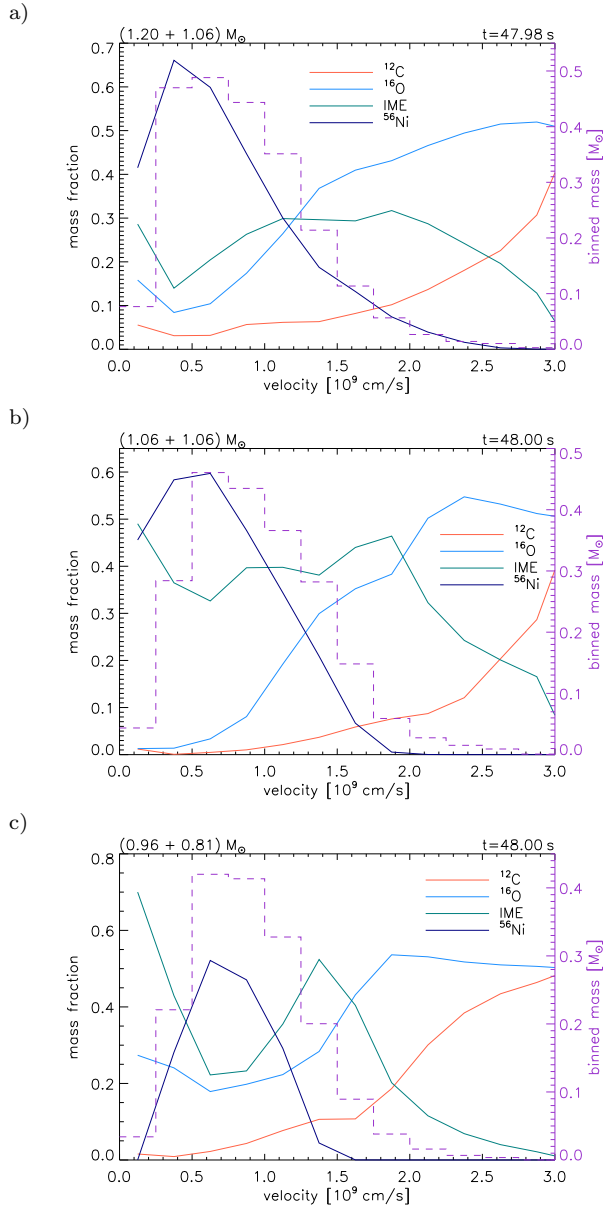


FIG. 4.— Mass fractions of different elements in bins of the ejecta velocity. ^{28}Si , ^{32}S , ^{36}Ar and ^{40}Ca are grouped together as “intermediate mass elements” (IME, green line). The total masses in the bins used to calculate the fractions are shown by the dashed magenta line (right-hand axis).

3.3. Ejecta Morphology

The 3D structures of the coasting ^{28}Si and ^{56}Ni ejecta are shown in Figure 5. In all cases, there is symmetry across the orbital plane. There is no axisymmetry around the line that connects the stars at the beginning of the detonation. The extent of the ^{28}Si and ^{56}Ni ejecta is anisotropic, reflecting that the ashes are accelerated most effectively in directions ahead of the primary (with respect to the global direction of rotation of the coalescing stars).

The ejecta of models 1.06 + 1.06 and 0.96 + 0.81 are morphologically very similar. The concave insides of the ^{56}Ni ejecta contain pockets of ^{28}Si as a result of burning in the secondary star. The fast-moving ^{28}Si surrounding the ^{56}Ni ejecta presumably originates from

the low-density outer parts of the primary star. Model 1.20 + 1.06 lacks most of this ^{28}Si “frame”.

The ejecta of unburnt fuel are shown in Figure 6. In models 1.06 + 1.06 and 0.96 + 0.81, a torus-shaped feature surrounds the connecting line on the side of the defunct secondary, with the fastest velocities in directions ahead of the secondary. We surmise that this is material expelled from the shock-heated secondary. The ejecta in model 1.20 + 1.06 form a preacher bench instead of a torus.

3.4. Direction-Dependence of Masses and Velocities

A quantitative representation of the ejecta is shown in Figure 8. The plots in the top row of each panel represent the solid angle mass densities of $^{12}\text{C}+^{16}\text{O}$, ^{28}Si and ^{56}Ni with respect to the coordinate origin. (Note that the actual center of the explosion, as defined by $\mathbf{v} = 0$ in the grid’s frame of reference, is virtually coincident with the coordinate origin at this stage. This is inevitable, because the explosion center does not move while the length scales increase.) The total masses listed in Table 3 can be retrieved by integrating over 4π . The orientation of the projection is sketched in Figure 7. The polar axis for each plot is chosen to be the line connecting the centers of the two stars (cf. Figure 1), with the “north pole” being on the side of the secondary. The prime meridian (thick blue line in the sketch) lies in the orbital plane ahead of the primary. Positive “longitudes” correspond to positive rotations according to the right-hand rule. The z -axis corresponds to $\pm 90^\circ$ longitude at the equator.

In all cases, the largest deposits of ^{28}Si are seen in directions behind the defunct primary star near the orbital plane. This ^{28}Si , which is moving slowly, corresponds to the central pocket inside the concave part of the ^{56}Ni ejecta shown in Figure 5. Fast ^{28}Si can be seen in other directions, albeit with much lower solid angle mass densities.

Large concentrations of ^{56}Ni are seen over a wide range of solid angles, including directions near the z -axis (normal to the orbital plane) and behind the defunct secondary star. The mass densities for the unburnt fuel, $^{12}\text{C}+^{16}\text{O}$, are in all cases high in directions ahead of the defunct secondary star near the orbital plane. These are the directions in which no ^{56}Ni and little ^{28}Si are seen.

3.5. Energetics

The total energy of the ejecta is positive in all cases (cf. Table 3), implying that there is enough energy for the ejecta to expand indefinitely. However, the spatial distribution of the energies could allow for a gravitational collapse in some local region. We investigated the possibility of gravitational fallback of an inner region onto the center of the explosion by calculating the total energy as a function of radius, using 100 radial bins. The gravitational binding energy is calculated to be

$$E_{\text{grav}}(r) = -\frac{1}{2}G \int_{V_r} dV \int_V dV' \frac{\rho(\mathbf{r})\rho(\mathbf{r}')}{|\mathbf{r} - \mathbf{r}'|}, \quad (1)$$

where the first integral includes only the volume within a sphere of radius r , here denoted as V_r , and the second

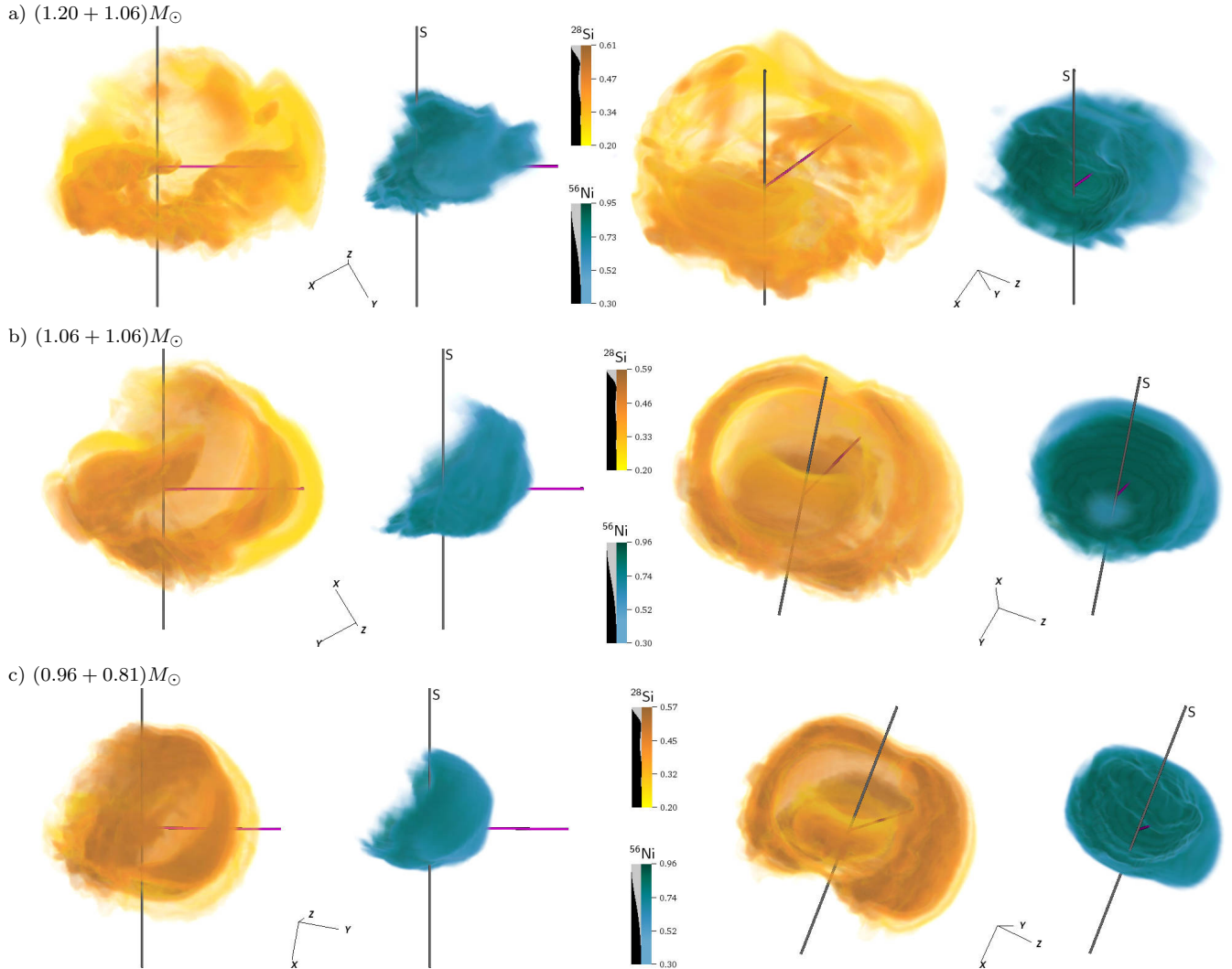


FIG. 5.— Volume renderings of the element mass fractions of ^{56}Ni (teal colors) and ^{28}Si (orange colors) in the homologously expanding ejecta, 48 seconds after the start of the detonation, at two different perspectives, respectively. The gray and magenta rods both lie in the orbital plane, intersecting at the origin (cf. Figure 1): the gray rod represents the line connecting the centers of the two WDs when the detonation sets off, and the magenta rod points in orthogonal direction away from the tidal tail of the primary. The side at which the secondary was is marked with an “S”. The perspective to the left corresponds to a face-on view of the orbital plane. To give a sense of scale: the distance from the origin to the respective outer tips of the rods is 10^{11} cm. The homologous expansion velocity at this distance is approximately 2.15×10^9 cm s $^{-1}$ in all cases shown.

integral includes the whole space⁶. We thus estimate that the potential fallback mass in all cases is insignificant, involving less than the innermost $10^{-3} M_{\odot}$.

The above estimate does not exclude gravitational fallback towards other points in the ejecta. An obvious candidate for such a point is the maximum of the inner integral in equation (1), which is located $\sim 10^{10}$ cm from the center (where the expansion velocity is $\sim 2.5 \times 10^8$ cm s $^{-1}$). We repeated the above calculations with r calculated around this point, using the kinetic energies measured by an observer who moves with this point. The potential fallback masses are again small, less than $0.02 M_{\odot}$ in all cases.

⁶ This may be overestimating the chance for a fallback. One could argue that the material at large radii ceases to contribute to the total potential once the expansion of the inner part slows down at the onset of a collapse, and the inner and outer parts become increasingly separated. The second integral would then have to include only V_r instead of V , and the energy needed to defy gravity would be less.

Note that in the above, we have ignored the energies from radioactive decay and electron recombination. The liberation of these latent energies could further decrease the chance for fallback. Also note that while our energetic argument suggests that considerable gravitational fallback is unlikely, only hydrodynamic calculations can definitely predict the long-term evolution of the ejecta.

4. LIGHT CURVES AND SPECTRA

We generated synthetic light curves and spectra of our merger models by post-processing the final output of the CASTRO hydrodynamical models with the radiative transfer code SEDONA (Kasen et al. 2006). The parameters of the transport calculations were equivalent to those of Kasen et al. (2009) and adopt the assumption of local thermodynamic equilibrium. While not strictly axially symmetric, the merger simulations do display a dominant axis of symmetry. The main dependence of the observables will therefore be on the polar viewing angle as measured from the main symmetry axis. For ease in

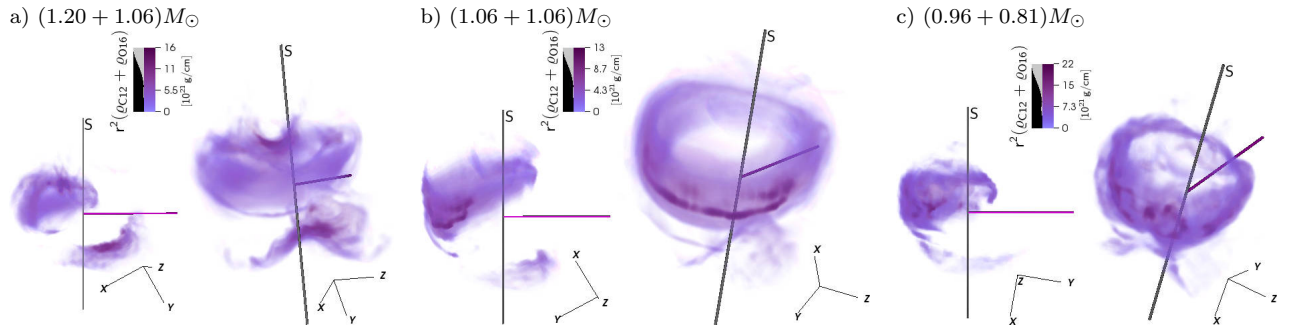


FIG. 6.— Volume renderings of the ejecta of ^{12}C and ^{16}O (unburnt fuel) in the homologously expanding ejecta, 48 seconds after the start of the detonation, at two different perspectives, respectively. The meaning of the rods is the same as in Figure 5, but for practical reasons, we here plot the density times the square of the distance to the origin (thus compensating for the increase of scales due to the expansion) instead of the mass fraction.

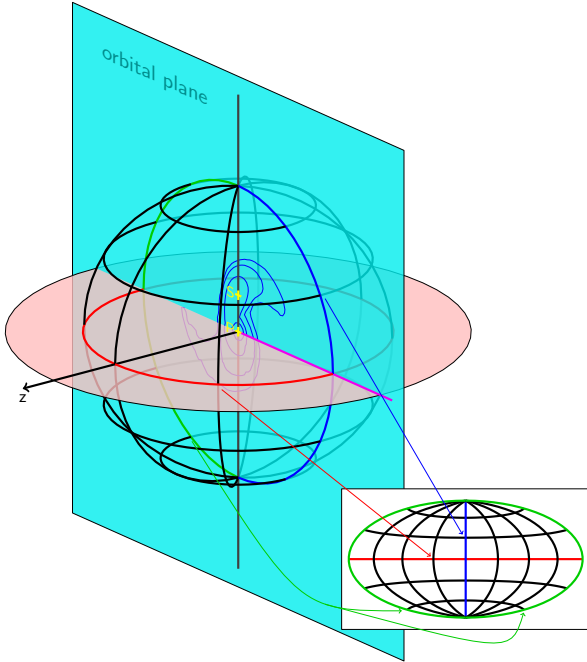


FIG. 7.— Sketch of the map projection used in Figure 8. The cyan plane, on which density contours of a merger are drawn in blue, corresponds to the orbital plane shown in Figure 1. Yellow crosses represent the centers of the merging stars. The gray and magenta lines correspond to the same-colored rods in Figures 5 and 6. In the map projection, they correspond to the polar axis and the direction of the prime meridian in the equatorial plane (shaded pink in the sketch), respectively.

analysis and computation, we azimuthally averaged the models into a 2D cylindrical coordinate system. This was done by integrating masses and momenta to obtain a grid with 128 radial and 256 vertical zones, with the assumed axis of symmetry defined as the line connecting the centers of the two stars when the detonation sets off.

Figure 9 illustrates the ejecta composition structure (plotted in velocity coordinates) for the azimuthally averaged model $0.96 + 0.81$. The geometry discussed in §3.3 is clearly visible in this 2D visualization, and will be useful for understanding the orientation dependencies of the light curves and spectra. The ^{56}Ni has bowl-like shape, and is most highly concentrated in a thin pancaked region in the lower polar region. The velocity of the ^{56}Ni in this lower polar region does not extend past $v \approx 6,000 \text{ km s}^{-1}$, whereas much higher ^{56}Ni ejection velocities ($v \approx 10,000 \text{ km s}^{-1}$) are seen the equatorial and

upper polar regions. The maximum IME ejection velocities are also lower in the lower pole ($v \approx 10,000 \text{ km s}^{-1}$) than the upper pole ($v \approx 15,000 \text{ km s}^{-1}$). The highest IME velocities are in the equatorial regions, where they extend to $v \approx 20,000 \text{ km s}^{-1}$. A pocket of IME also exists near zero velocity, due to burning of the secondary WD, and a pocket of low-velocity oxygen is visible as well.

4.1. Synthetic Light Curves

Figure 10 shows the synthetic bolometric light curves, as a function of the polar viewing angle, for each of the 3 merger models. Due to the strong ejecta asymmetry, the peak luminosity varies by a factor of nearly 2 or more with orientation. For model $0.96 + 0.81$, the mean peak bolometric luminosity (averaged over all polar angles) is $L_{\text{bol}} = 1.32 \times 10^{43} \text{ ergs s}^{-1}$, comparable to that of normal SNe Ia. However, for polar viewing angles near $\theta = 180^\circ$ – i.e., looking up along the z-axis in Figure 9 – the light curve is significantly over-luminous, peaking at $2 \times 10^{43} \text{ ergs s}^{-1}$. The anisotropy of the radiation is due to the overabundance of ^{56}Ni in the lower polar region, which results in a greater energy deposition on one side of the ejecta, and a preferential escape of photons in the downward direction. The same orientation effects are present in the more massive merger models, $1.06 + 1.06$ and $1.20 + 1.06$, which have higher total ^{56}Ni masses and larger mean peak bolometric luminosities, $L_{\text{bol}} = 1.69 \times 10^{43} \text{ ergs s}^{-1}$ and $L_{\text{bol}} = 1.77 \times 10^{43} \text{ ergs s}^{-1}$ respectively. These two models are slightly over-luminous from most viewing angles, and from the $\theta \approx 180^\circ$ they are extraordinarily bright, $L_{\text{bol}} \approx 3 \times 10^{43} \text{ ergs s}^{-1}$, comparable to the values seen in the rare class of so-called “super-Chandrasekhar” mass events (Howell et al. 2006; Hicken et al. 2007; Scalzo et al. 2010; Taubenberger et al. 2011; Silverman et al. 2011).

Closer inspection of the synthetic light curves reveals that a large fraction of the total luminosity is emitted in the ultraviolet bands ($\lambda \lesssim 3500 \text{ \AA}$), and that the optical B-band light curves have somewhat more moderate peak luminosities and orientation effects (Figure 11). In model $0.96 + 0.81$, the peak B-band magnitude varies by about 0.5 mag with polar angle, from $M_B = -19.3$ at $\theta = 180^\circ$ to $M_B \approx -18.8$ at $\theta \lesssim 90^\circ$. This is within the range of normal SNe Ia. The peak B-band magnitudes of models $1.06 + 1.06$ and $1.20 + 1.06$ show a similar degree of variation, reaching maximum values of $M_B \approx -19.8$ for $\theta = 180^\circ$. These brightest values are similar to,

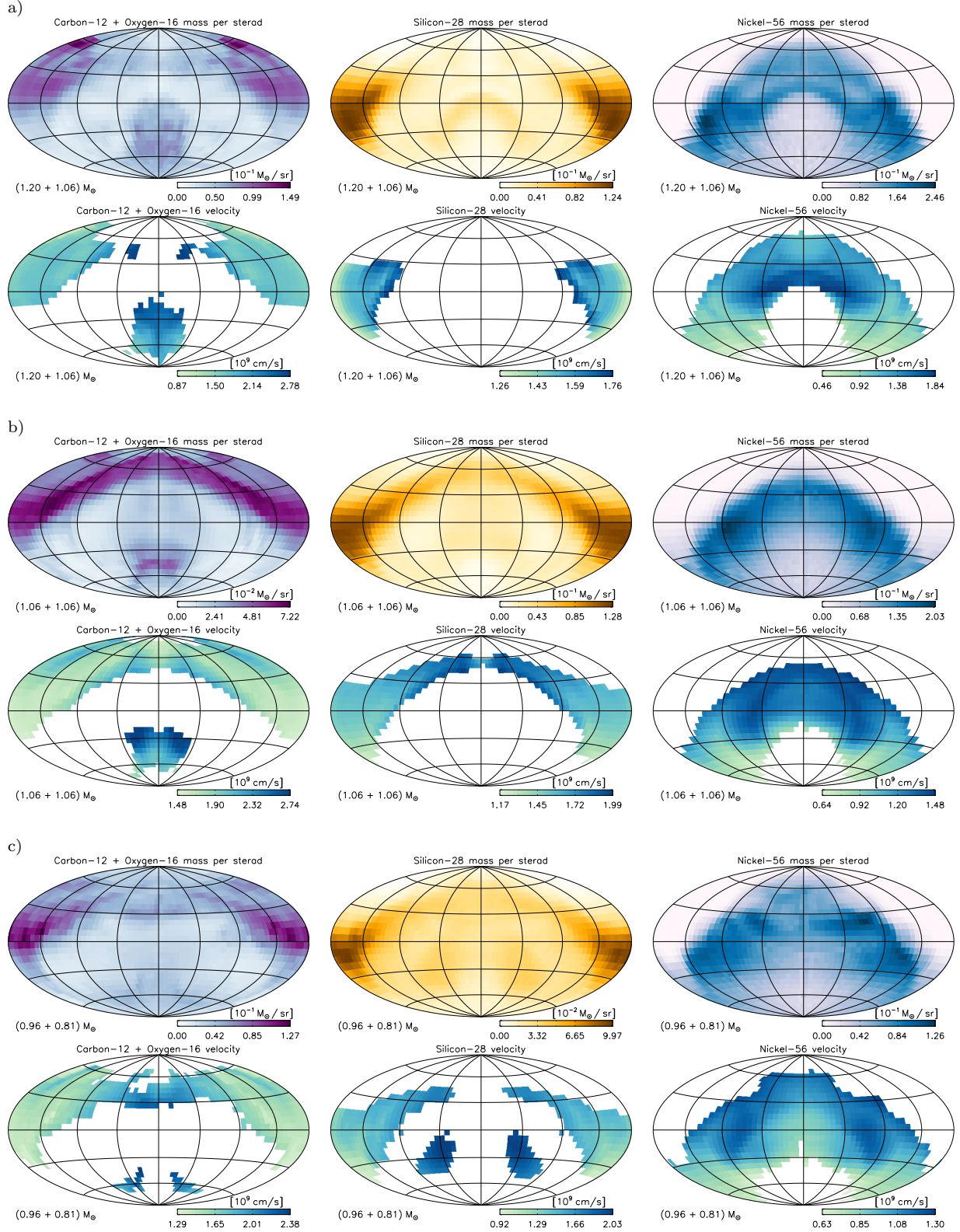


FIG. 8.— *Top row of each panel:* $^{12}\text{C}+^{16}\text{O}$ (purple colors), ^{28}Si (orange colors) and ^{56}Ni (blue colors) masses per unit of solid angle as a function of spatial direction with respect to the explosion center in a Hammer projection. See Figure 7 and §3.4 for details on the orientation of the projection. *Bottom row of each panel:* Corresponding ejecta velocities, measured at the smallest radius that contains 95% of the mass in a given solid angle bin. The velocities are only plotted for directions in which the mass density is at least one third of the maximum (corresponding to the second label from the left in the color bar of the respective mass density plot).

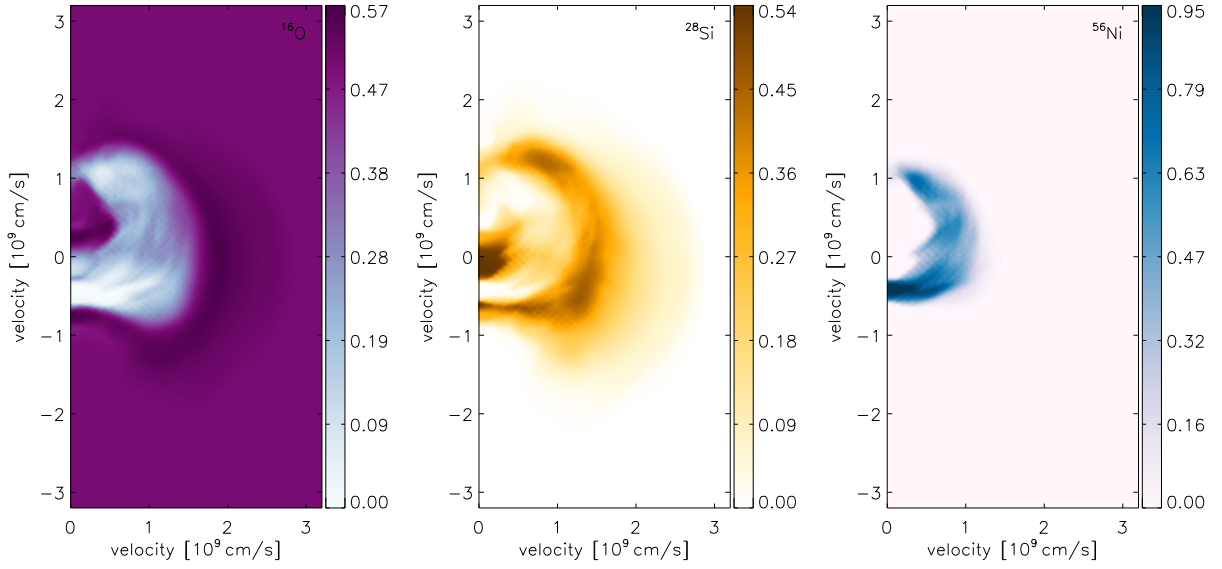


FIG. 9.— Compositional structure in the azimuthally averaged version of model 0.96+0.81. The color coding shows the mass fractions of oxygen, silicon, and radioactive nickel.

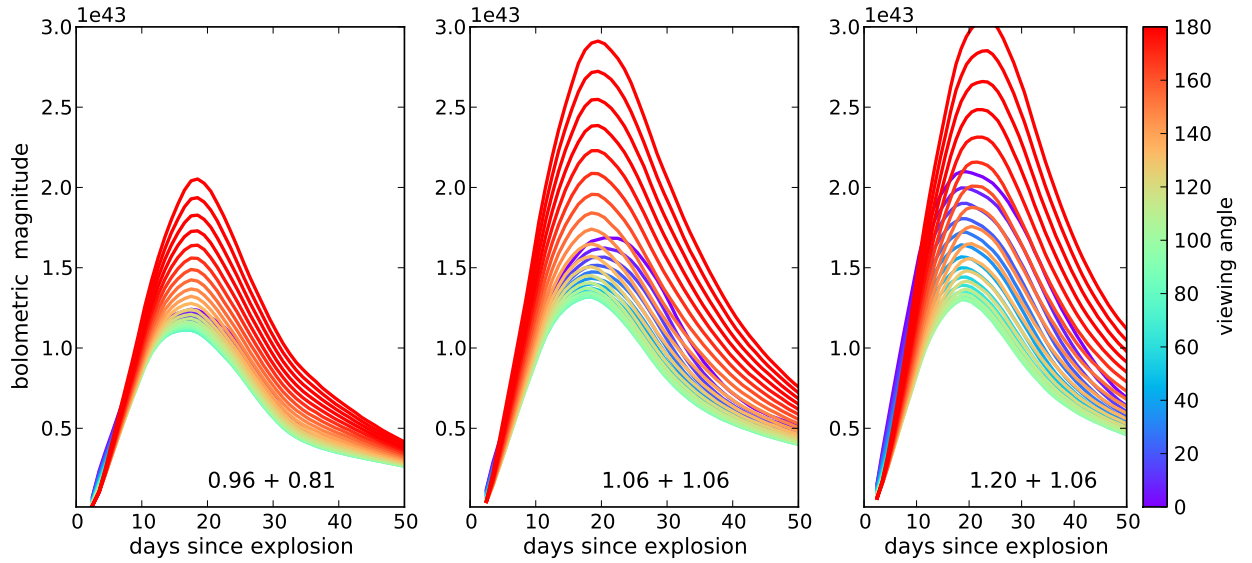


FIG. 10.— Synthetic bolometric light curves of the merger models. The color coding indicates the polar viewing angle.

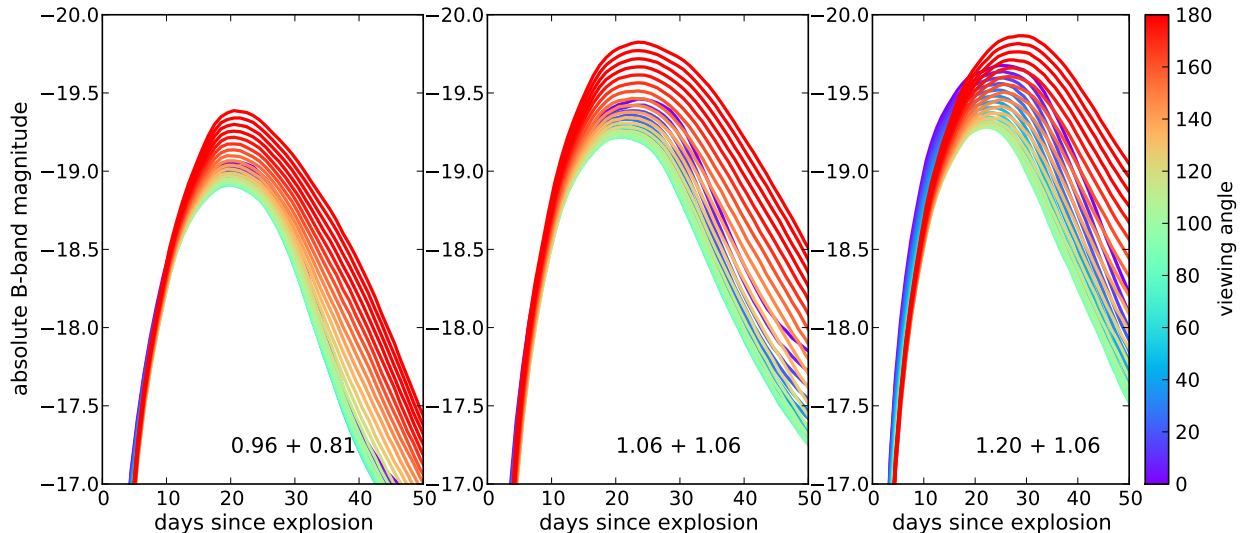


FIG. 11.— Synthetic B-band light curves of the merger models. The color coding indicates the polar viewing angle.

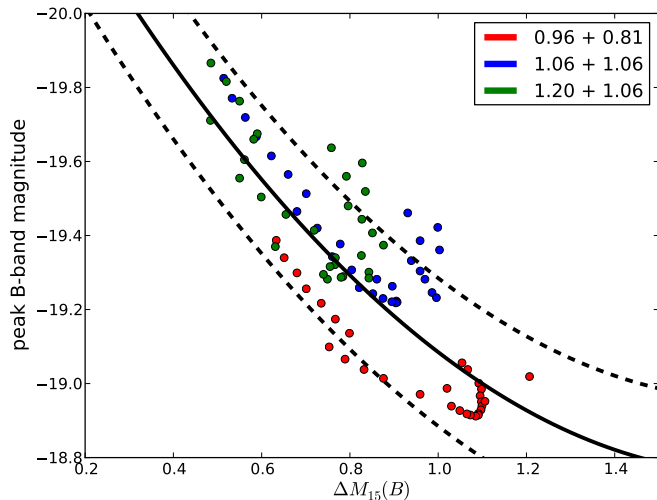


FIG. 12.— Width-luminosity relation of the models. The y-axis is the measured peak B-band absolute magnitude and the x-axis is the decline in magnitudes from B-band peak to 15 days later. The individual points for each model represent different polar viewing angles. The black lines show the relation from Phillips et al. (1999), $M_B = M_{B,0} + 0.786(\Delta M_{15}(B) - 1.1) - 0.633(\Delta M_{15}(B) - 1.1)^2$. The solid line uses $M_{B,0} = -19.0$, while the upper and lower dashed lines use $M_{B,0} = -19.2$ and $M_{B,0} = -18.8$, respectively.

though a bit lower than those observed for the “super-Chandrasekhar” SNe Ia, which are measured in the range $M_B = -19.9$ to -20.2 mag (Taubenberger et al. 2011).

Figure 12 shows the width luminosity relation (WLR) of the model light curves, plotted as the correlation between the peak B-band absolute magnitude and the B-band decline rate, $\Delta M_{15}(B)$. The individual points for a given model represent different viewing angles, and are seen to generally follow the observed “broader equals brighter” trend. This behavior is notable, given that in other asymmetric models (in particular, realizations of Chandrasekhar mass delayed-detonation explosions) orientation effects generally led to deviations from the WLR (Kasen & Plewa 2007; Kasen et al. 2009; Sim et al. 2013). The rough WLR trend obeyed by each model in Figure 12 can likely be explained by the distribution of ^{56}Ni found in these merger simulations. Because the velocity of ^{56}Ni is lowest in the lower polar regions, the line

blanketing from iron group elements is minimal when the SN is observed near $\theta \approx 180^\circ$. This reduced degree of line blanketing at blue wavelengths results in a slower B-band decline rate when observed from $\theta \approx 180^\circ$. We note that the bolometric light curves of the individual models do not obey a strong WLR (Figure 10), indicating that the B-band WLR relation of Figure 12 is indeed attributable to color evolution effects (Kasen & Woosley 2007).

In detail, the model WLR relation resembles the observed one of Phillips et al. (1999) with an assumed normalization of $M_B = -19.0$ at $\Delta M_{15}(B) = 1.1$. The scatter in the model relation is ≈ 0.2 mag, which is comparable to, but slightly larger than that of the observed sample without additional (e.g., color) corrections. Given the relatively high masses considered in our merger simulations, the models do not populate the fast declining range of the plot ($\Delta M_{15}(B) > 1.2$) and are heavily weighted to broader light curve events. The brightest model realizations have $M(B) = -19.8$ and decline very slowly, $\Delta M_{15}(B) \approx 0.5$ – 0.6 . While these model points lie along the extrapolation of the Phillips et al. (1999) relation, the observed over-luminous “super-Chandrasekhar” SNe Ia generally do not, having instead slightly faster decline rates, $\Delta M_{15}(B) \approx 0.6$ – 0.8 (Taubenberger et al. 2011).

4.2. Synthetic Spectra

Figure 13 shows synthetic spectra, as observed at peak brightness, of each of the merger models. The strong viewing angle dependencies are apparent, and are most dramatic at bluer wavelengths. For model $0.96 + 0.81$, the variation in the B-band flux ($\lambda \approx 4500 \text{ \AA}$) is a factor of ≈ 1.5 , while in the U-band ($\lambda \approx 3500 \text{ \AA}$) the variation is more than a factor of 2. In the ultraviolet (UV) region of the spectrum the flux varies with viewing angle by nearly a factor of 10. Qualitatively similar orientation effects are seen in the synthetic spectra of models $1.06 + 1.06$ and $1.20 + 1.06$. A similar variation in the B- and U-band flux with viewing angle can be seen in the merger simulations presented by Röpke et al. (2012).

The strong orientation effects of the model spectra can be understood, to first order, by line blanketing effects. The emission at blue wavelengths is strongly influenced

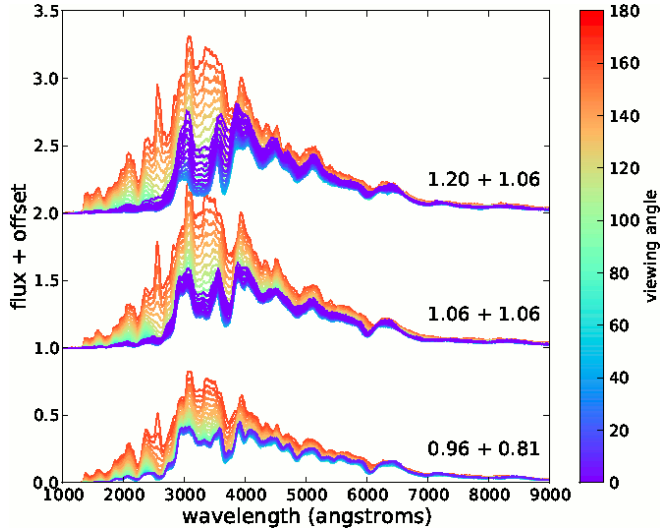


FIG. 13.— Synthetic spectra at peak brightness for the models. The spread for each model shows the range of variation with viewing angle.

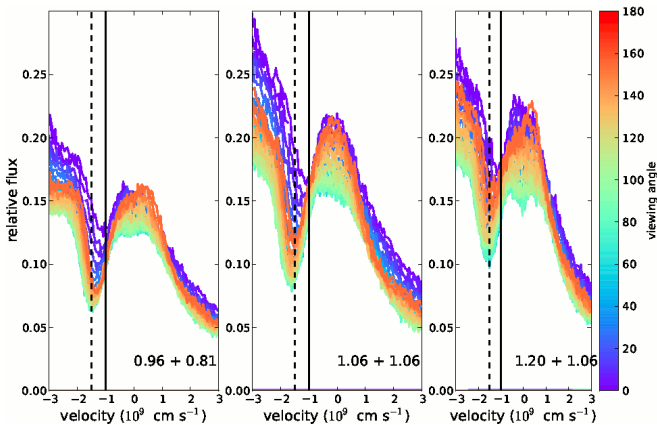


FIG. 14.— Zoom in of the spectral region around the Si II absorption feature, as seen from different viewing angles, for the models observed at peak mean B-band brightness. The x-axis shows the velocity relative to the Si II gf-weighted rest wavelength of 6355 Å. The solid and dashed lines, mark velocities of 10,000 km s⁻¹ and 15,000 km s⁻¹, respectively. A C II absorption feature is visible near zero Si II velocity in models 0.96 + 0.81 and 1.20 + 1.06.

by the opacity of millions of blended, Doppler shifted iron group lines, which are more highly concentrated at blue and ultraviolet wavelengths. In the lower polar regions of the ejecta, the synthesized iron group (namely ⁵⁶Ni) is restricted to a narrow range of velocities near $v \lesssim 6000$ km s⁻¹, which is low compared to standard SN Ia models like W7 (Nomoto et al. 1984). When viewed from polar angles near $\theta = 180^\circ$, the line blanketing by iron group elements is therefore reduced, and the emergent spectrum is significantly bluer. From other angles, the ⁵⁶Ni is distributed across a greater range of velocities, and so provides higher line blanketing and redder colors. A similar effect of an asymmetric distribution ⁵⁶Ni on SN Ia colors was discussed in Foley & Kasen (2011).

The geometrical distribution of the IMEs also has an influence on the spectral line features seen at maximum light. Because the IMEs have lower ejecta velocities in the lower polar region, the absorption features of silicon, sulfur and calcium lines all show lower Doppler shifts when observed from $\theta \approx 180^\circ$. Figure 14 shows a zoom

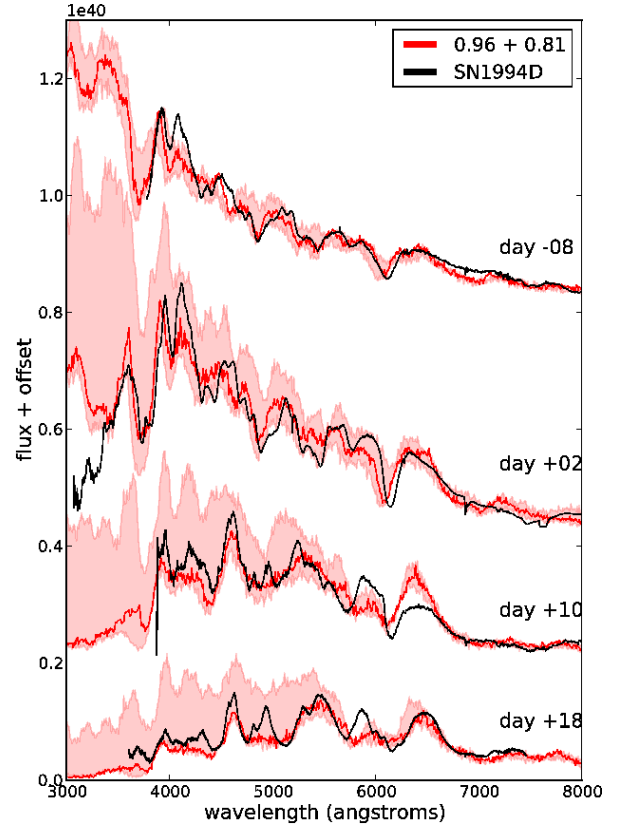


FIG. 15.— Synthetic spectral time series for model 0.96 + 0.81, compared to observations of the normal Type Ia SN 1994D. The shaded red region shows the range of variation with viewing angle, and the solid red line marks the equatorial $\theta = 90^\circ$ viewing angle. We have normalized the model spectrum at each epoch independently to provide an optimal comparison to the observed spectral features.

in of the hallmark Si II feature (gf-weighted rest wavelength 6355 Å). At peak brightness, the velocity as measured from the minimum of the Si II absorption feature varies by $\sim 40\%$, from 10,000 km s⁻¹ from $\theta = 180^\circ$ to 14,000 km s⁻¹ from other angles.

Clear carbon absorption features from C II are also visible near the emission peak of the 6355 Å Si II feature in the maximum light spectra of models 0.96 + 0.81 and 1.20 + 1.06 (Figure 14). This is a result of the relatively large unburned carbon masses ($\sim 0.1 M_\odot$) left over from the secondary star. In the equal mass ratio merger 1.06 + 1.06, less carbon remained unburned ($\sim 5 \times 10^{-2} M_\odot$) and the C II absorption is less obvious at these epochs. The strength of the C II absorption varies with viewing angle, given the asymmetric distribution of carbon in the ejecta. Carbon lines have been detected in normal SNe Ia (Branch et al. 2003; Thomas et al. 2011; Silverman & Filippenko 2012). In addition, “super-Chandrasekhar” SNe Ia frequently show significantly stronger C II absorption.

On the whole, the synthetic spectra of our merger simulations resemble those of normal SNe Ia. Figure 15 compares the synthetic spectral time series of model 0.96 + 0.81 to observations of SN 1994D (Höflich 1995; Meikle et al. 1996; Patat et al. 1996). Most of the major spectral features are reproduced, although discrepancies can be noticed in the depth and velocity of individual line profiles. Similar spectral fits were shown for the 1.1 + 0.9

violent merger model of Pakmor et al. (2011) and Röpke et al. (2012). The overall quality of the fits is comparable to that found for multi-dimensional delayed detonation explosions of Chandrasekhar mass WDs (Kasen et al. 2009; Röpke et al. 2012; Sim et al. 2013). The dispersion with viewing angle, however, is more extreme in the merger model spectra, especially at UV wavelengths. This is not surprising given the greater ejecta asymmetry.

5. SUMMARY AND DISCUSSION

The merging of WDs was simulated for three different pairings of progenitor masses, and the disruption of these systems by thermonuclear detonations set off during the merging process was studied. All of the models considered generated energetic explosions with high yields of ^{56}Ni and substantial amounts of IMEs, in particular ^{28}Si and ^{32}S . The secondary star, which had shed mass and was stretched by tidal forces at the time of ignition, contributed to the nucleosynthesis of IMEs. In addition, it ejected significant amounts of unburnt fuel.

The morphology of the ejecta was quite complex in general. The presence of the companion star naturally breaks the spherical symmetry, presumably more so than the non-central ignition. In the rotating system of coalescing WDs, the density drops more rapidly ahead of the primary star, making the acceleration of the ashes more efficient in this direction. This breaks the axisymmetry about the line connecting the two stars. Even though the rotational speed is very slow compared to the detonation, it leaves an imprint on the ejecta. The high energies in the ejecta suggest that they will not be subject to long-term gravitational interaction and that their asymmetry will be retained indefinitely.

The total yields found in our calculations confirm that the violent mergers of WDs can produce the nucleosynthesis needed for SNe Ia. However, not all kinds of pairings of WDs produce SNe Ia such like those that are observed. This raises the question as to why nature would favor certain systems over others. We expect mergers involving high-mass WDs to be rare for the simple fact that high-mass WDs are rare. Our $1.20 + 1.06$ model with carbon-oxygen composition clearly falls into this category. However, it has been argued that the WD primary may be able to grow via accretion during the binary evolution Ruiter et al. 2013. On the other hand, mergers of low-mass WDs probably do not produce the necessary thermonuclear runaway that leads to a detonation. The ignition of the $(0.96 + 0.81)M_{\odot}$ merger in this work is marginal and uncertain. We had to artificially induce a detonation to make it work. We also considered a $(1.06 + 0.64)M_{\odot}$ merger, but that model did not reach the necessary detonation condition (this model is instead presented in Raskin et al. 2013, with a detonation being manually triggered in the post-merger state). It seems fair to assume that models with lighter primaries in combination with a $\sim 0.64 M_{\odot}$ secondary will also fail to ignite a prompt explosion. Detonations in merging WDs with masses lighter than in our $0.96 + 0.81$ model may therefore be unrealistic, unless the ignition is aided by additional factors such as the presence of helium (Pakmor et al. 2013). Our findings are in line with a recent study by Dan et al. (2013) that suggests a minimum total mass of $2.1 M_{\odot}$ for detonation in carbon-oxygen merger systems, a condition satisfied only by our two heaviest

models.

Another possible reason for diversity besides progenitor masses could be a spread in the time when the detonation conditions are reached. It is not clear whether the evolutionary state at the time of the detonation is robustly always the same for a similar pair of WD masses. For instance, the $1.06 M_{\odot}$ secondary in combination with a $1.20 M_{\odot}$ primary has shed more mass than in combination with a $1.06 M_{\odot}$ primary when the detonation sets off. Would the state of the $1.06 M_{\odot}$ secondary in combination with a $1.12 M_{\odot}$ primary lie in-between these two models? Our simulations suggest that these details could have an effect on the production of IMEs as well as on the ejecta morphology. Many more models would have to be calculated to cover the possible parameter space.

The synthetic light curves and spectra of our $0.96 + 0.81$ merger model generally resemble those of normal SNe Ia. Our results are similar to those of Pakmor et al. (2012b), who also found a favorable comparison to observation in a $1.1 + 0.9$ merger model. Despite the smaller primary mass in our model, the total amount of ^{56}Ni synthesized ($M_{\text{Ni}} = 0.58 M_{\odot}$) was only slightly lower than that of Pakmor et al. (2012b) ($M_{\text{Ni}} = 0.616 M_{\odot}$). This is most likely due to the different tables used to calculate the nucleosynthesis in a detonation (see Table 2). In general, our simulations predict greater ^{56}Ni yields, which if correct would imply that slightly lower mass WDs are sufficient for producing normal SNe Ia. The B-band light curve of our $0.96 + 0.81$ model has a mean (i.e., averaged over all viewing angles) peak magnitude of $M_B = -19$, a rise time of $t_B = 20$ days, and a decline rate of $\Delta M_B(15) = 1.0$ mag, values which are very similar to those found in the $1.1 + 0.9$ model of Pakmor et al. (2012b).

We have also considered the observables of violent mergers consisting of more massive progenitors, namely $1.06 + 1.06$ and $1.20 + 1.06$. These models produced more ^{56}Ni ($0.86 M_{\odot}$ and $0.99 M_{\odot}$, respectively) and will yield over-luminous SNe Ia. Such events may be interesting in the context of the very-luminous, “super-Chandrasekhar” SNe Ia. Due to the asymmetry of the ejecta, the brightness of these merger models is boosted when viewed from certain viewing angles (namely, those for which the bulk of the ^{56}Ni is closer to the observer). As a result, models with a primary WD near or just $1.2 M_{\odot}$ can, for some orientations, reach comparable brightness to the observed events, even though the ^{56}Ni masses are lower than what has been empirically inferred on the basis of 1D models. (Hillebrandt et al. 2007) had previously suggested, in a different context, that asymmetry of the ejecta may reduce the ^{56}Ni required to explain the “super-Chandrasekhar” SNe Ia. From the brightest orientations ($\theta \approx 0^\circ$) the $1.20 + 1.06$ model also shows a slow light curve decline, a notable CII absorption feature, and relatively lower SiII absorption line velocities, all qualitatively consistent with what is seen in the observed events.

These violent merger models show strong variations with viewing angles. These are primarily due to the aspherical distribution of ^{56}Ni , which leads to both variations of the brightness and the degree of line blanketing with viewing angle. The range of variation in the ultraviolet is most extreme, with order of magnitude flux

variations seen. SNe Ia do show the greatest degree of diversity at ultraviolet wavelengths, however the observed dispersion in peak UV magnitude is not as large as in the models (Brown et al. 2010; Cooke et al. 2011). We have also constructed a WLR for the violent merger models and showed that, despite the strong dispersion of observables with viewing angle, the models roughly lie along the observed trend.

Although the synthetic light curves and spectra we have calculated here are generally consistent with observations of SNe Ia, there may be other observables of the models that are in conflict. In particular, the strong global asymmetry may lead to high levels of polarization, which would be inconsistent with the generally low continuum polarization found in observations (see Wang & Wheeler 2008, and references therein). In addition, the unusual chemical distribution of the ejecta, with a pocket of inner oxygen surrounded by an outer bowl of ^{56}Ni , may not be consistent with nebular spectra of SNe Ia, which typically show only moderately asymmetric iron group lines and no nebular oxygen emission. Additional calculations will be needed to explore these features and compare to observations.

We have also considered a late (post-merger) detonation of model $0.96 + 0.81$, details of which are presented in Raskin et al. (2013), and found higher ^{56}Ni and lower

IME yields as in the early (peri-merger) detonation presented here. The biggest difference, however, lies in the morphology of the ejecta. This morphology could well be the decisive factor to determine whether the double degenerate scenario is viable, and whether the detonation happens during or after the merging process.

This research has been supported by the DOE HEP Program under contract DE-SC0010676; the National Science Foundation (AST 0909129 and AST 1109896) and the NASA Theory Program (NNX09AK36G). DK is supported by a Department of Energy Office of Nuclear Physics Early Career Award (DE-SC0008067). RM acknowledges support by the Alexander von Humboldt Foundation through the Feodor Lynen Research Fellowship program. We thank John Bell and Ann Almgren for their major roles in developing the CASTRO code. This research used resources of the National Energy Research Scientific Computing Center, which is supported by the Office of Science of the U.S. Department of Energy under Contract No. DE-AC02-05CH11231. This research used resources of the Oak Ridge Leadership Computing Facility at the Oak Ridge National Laboratory, which is supported by the Office of Science of the U.S. Department of Energy under Contract No. DE-AC05-00OR22725.

REFERENCES

- Almgren, A. S., Beckner, V. E., Bell, J. B., et al. 2010, *ApJ*, 715, 1221
- Benz, W., Cameron, A. G. W., Press, W. H., & Bowers, R. L. 1990, *ApJ*, 348, 647
- Branch, D., Garnavich, P., Matheson, T., et al. 2003, *AJ*, 126, 1489
- Brown, P. J., Roming, P. W. A., Milne, P., et al. 2010, *ApJ*, 721, 1608
- Cooke, J., Ellis, R. S., Sullivan, M., et al. 2011, *ApJ*, 727, L35
- Dan, M., Rosswog, S., Brueggen, M., & Podsiadlowski, P. 2013, 1308.1667 [astro-ph.HE]
- Dan, M., Rosswog, S., Guillochon, J., & Ramirez-Ruiz, E. 2012, *MNRAS*, 422, 2417
- Fink, M., Hillebrandt, W., & Röpke, F. K. 2007, *A&A*, 476, 1133
- Fink, M., Röpke, F. K., Hillebrandt, W., et al. 2010, *A&A*, 514, A53
- Foley, R. J., & Kasen, D. 2011, *ApJ*, 729, 55
- Fryer, C. L., Rockefeller, G., & Warren, M. S. 2006, *ApJ*, 643, 292
- Guerrero, J., García-Berro, E., & Isern, J. 2004, *A&A*, 413, 257
- Hicken, M., Garnavich, P. M., Prieto, J. L., et al. 2007, *ApJ*, 669, L17
- Hillebrandt, W., & Niemeyer, J. C. 2000, *ARA&A*, 38, 191
- Hillebrandt, W., Sim, S. A., & Röpke, F. K. 2007, *A&A*, 465, L17
- Höflich, P. 1995, *ApJ*, 443, 89
- Howell, D. A., Sullivan, M., Nugent, P. E., et al. 2006, *Nature*, 443, 308
- Iben, Jr., I., & Tutukov, A. V. 1984, *ApJS*, 54, 335
- Kasen, D., & Plewa, T. 2007, *ApJ*, 662, 459
- Kasen, D., Röpke, F. K., & Woosley, S. E. 2009, *Nature*, 460, 869
- Kasen, D., Thomas, R. C., & Nugent, P. 2006, *ApJ*, 651, 366
- Kasen, D., & Woosley, S. E. 2007, *ApJ*, 656, 661
- Lorén-Aguilar, P., Isern, J., & García-Berro, E. 2009, *A&A*, 500, 1193
- Marsh, T. R., Nelemans, G., & Steeghs, D. 2004, *MNRAS*, 350, 113
- Meikle, W. P. S., Cumming, R. J., Geballe, T. R., et al. 1996, *MNRAS*, 281, 263
- Moll, R., & Woosley, S. E. 2013, *ApJ*, 774, 137
- Nomoto, K., Thielemann, F.-K., & Yokoi, K. 1984, *ApJ*, 286, 644
- Pakmor, R., Edelmann, P., Röpke, F. K., & Hillebrandt, W. 2012a, *MNRAS*, 424, 2222
- Pakmor, R., Hachinger, S., Röpke, F. K., & Hillebrandt, W. 2011, *A&A*, 528, A117
- Pakmor, R., Kromer, M., Röpke, F. K., et al. 2010, *Nature*, 463, 61
- Pakmor, R., Kromer, M., & Taubenberger, S. 2013, ArXiv e-prints
- Pakmor, R., Kromer, M., Taubenberger, S., et al. 2012b, *ApJ*, 747, L10
- Patat, F., Benetti, S., Cappellaro, E., et al. 1996, *MNRAS*, 278, 111
- Phillips, M. M., Lira, P., Suntzeff, N. B., et al. 1999, *AJ*, 118, 1766
- Raskin, C., Scannapieco, E., Fryer, C., Rockefeller, G., & Timmes, F. X. 2012, *ApJ*, 746, 62
- Raskin, C., et al. 2013, *ApJ* submitted
- Röpke, F. K., Kromer, M., Seitenzahl, I. R., et al. 2012, *ApJ*, 750, L19
- Ruiter, A. J., Belczynski, K., Sim, S. A., et al. 2011, *MNRAS*, 417, 408
- Ruiter, A. J., Sim, S. A., Pakmor, R., et al. 2013, *MNRAS*, 429, 1425
- Scalzo, R. A., Aldering, G., Antilogus, P., et al. 2010, *ApJ*, 713, 1073
- Seitenzahl, I. R., Meakin, C. A., Townsley, D. M., Lamb, D. Q., & Truran, J. W. 2009, *ApJ*, 696, 515
- Shen, K. J., & Bildsten, L. 2013, 1305.6925 [astro-ph.HE]
- Silverman, J. M., & Filippenko, A. V. 2012, *MNRAS*, 425, 1917
- Silverman, J. M., Ganeshalingam, M., Li, W., et al. 2011, *MNRAS*, 410, 585
- Sim, S. A., Fink, M., Kromer, M., et al. 2012, *MNRAS*, 420, 3003
- Sim, S. A., Seitenzahl, I. R., Kromer, M., et al. 2013, *MNRAS*, 436, 333
- Taubenberger, S., Benetti, S., Childress, M., et al. 2011, *MNRAS*, 412, 2735
- Thomas, R. C., Aldering, G., Antilogus, P., et al. 2011, *ApJ*, 743, 27
- Timmes, F. X., & Arnett, D. 1999, *ApJS*, 125, 277
- Timmes, F. X., & Swesty, F. D. 2000, *ApJS*, 126, 501
- Wang, L., & Wheeler, J. C. 2008, *ARA&A*, 46, 433
- Webbink, R. F. 1984, *ApJ*, 277, 355
- Woosley, S. E., & Kasen, D. 2011, *ApJ*, 734, 38
- Yoon, S.-C., Podsiadlowski, P., & Rosswog, S. 2007, *MNRAS*, 380, 933
- Zhang, W., Howell, L., Almgren, A., Burrows, A., & Bell, J. 2011, *ApJS*, 196, 20

Zhu, C., Chang, P., van Kerkwijk, M. H., & Wadsley, J. 2013,
ApJ, 767, 164